JOURNAL OF GEOPHYSICAL RESEARCH, VOL. 100, NO. B7, PAGES 12,951–12,958, JULY 10, 1995

Magnetic and electric fields associated with changes in high pore pressure in fault zones: Application to the Loma Prieta ULF emissions

Mark A. Fenoglio
Geophysics Department, Stanford University, Stanford, California

Malcom J. S. Johnston and Jim D. Byerlee
U.S. Geological Survey, Menlo Park, California

Abstract. We determined the electric and magnetic fields generated during failure of faults containing sealed compartments with pore pressures ranging from hydrostatic to lithostatic levels. Exhumed fault studies and strain measurement data limit the possible size of these compartments to less than 1 km in extent. Rupture of seals between compartments produces rapid pore pressure changes and fluid flow and may create fractures that propagate away from the high-pressure compartment, along the fault face. Nonuniform fluid flow results from pressure decrease in the fracture from crack-generated dilatancy, partial blockage by silica deposition, and clearing as pressure increases. A direct consequence of this unsteady fluid flow may be associated transient magnetic signals caused by electrokinetic, piezomagnetic, and magnetohydrodynamic effects. Models of these processes for fault geometries with 1-km-high pressure compartments show that electrokinetic effects are several orders of magnitude larger than the other mechanisms. The electrokinetic signals produced by this unsteady flow are comparable in magnitude and frequency to the magnetic signals observed prior to the M_L 7.1 Loma Prieta earthquake of October 18, 1989, provided fracture lengths are less than 200 m.

Introduction

Byerlee [1990, 1992] and *Rice* [1992] recently suggested a resolution of the "San Andreas heat flow paradox" by proposing a model in which fluid pressure gradients within the fault zone can produce a fault with low strength while avoiding hydrofracture in the surrounding rock due to excessive fluid pressure. *Byerlee* [1993] extended this idea by suggesting that silica deposition within the fault zone and between the fault zone and the country rock results in the formation of sealed compartments of various sizes and porosities. Compaction increases the fluid pressure to levels that are greater than hydrostatic but not uniform from compartment to compartment along the fault.

The formation, growth, and failure of these high-pressure compartments have interesting consequences, particularly for fault mechanics and earthquake prediction research. Changing pore pressure from perhaps lithostatic to hydrostatic in these inclusions should, depending on their size and location, generate readily detectable strain changes, microseismicity, and electric and magnetic field transients prior to fault failure. Observations of high-resolution strain before moderate earthquakes [*Johnston et al.*, 1987], microearthquake patterns [*Nadeau et al.*, 1994], and indications from exhumed faults suggest that characteristic compartment sizes could not be larger than 100 m to 1000 m in extent [*Johnston*, 1994]. Aseismic failure of these inclusions could provide the trigger mechanism for larger-scale sonic fault rupture (conventional earthquakes).

Our primary interest here concerns magnetic and electric fields that might result from mechanisms initiated by rapid pore pressure changes and fluid flow following rupture or partial rupture of these compartments. These mechanisms include electrokinetic effects [*Mizutani et al.*, 1976; *Fitterman*, 1978, 1979; *Ishido and Mizutani*, 1981; *Miyakoshi*, 1986; *Dobrovolsky et al.*, 1989], piezomagnetic effects [*Stacey*, 1964; *Stacey and Johnston*, 1972; *Sasai*, 1980; *Johnston*, 1989], and possible contributions from magnetohydrodynamic effects [*Draganov et al.*, 1991] and stress-resistivity changes [*Mazella and Morrison*, 1974; *Fitterman and Madden*, 1977; *Madden*, 1979; *Morrison et al.*, 1979; *Qian et al.*, 1983; *Sheng and Chen*, 1988; *Park and Fitterman*, 1990]. In this paper we investigate comparative electrokinetic, piezomagnetic, and magnetohydrodynamic models and realistic extensions of these models, expected from the simple "compartment failure" hypothesis. In particular, we suggest that magnetic fields resulting from irregular fluid flow should be expected given the dramatic physical changes during compartment failure. Further, these effects at the hypocenter of the 1989 M_L 7.1 Loma Prieta earthquake may be responsible for the increased ULF noise reported by *Fraser-Smith et al.* [1990] near the epicenter before and after the earthquake.

Paper number 95JB00076.
0148-0227/95/95JB-00076$05.00

High Pore Pressure Fault Model

In *Byerlee*'s [1993] model of high fault zone pressure, impermeable seals hydrologically isolate the fault zone from the surrounding country rock. A three-dimensional network

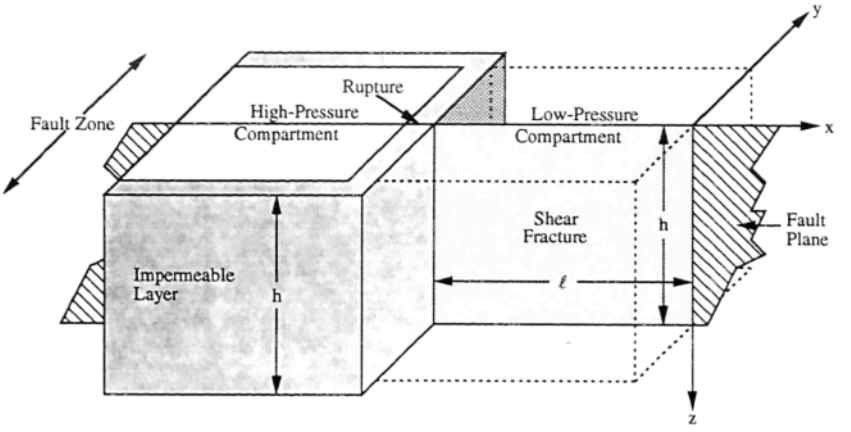

Figure 1. Geometry of the *Byerlee* [1993] compartment model. The shear fracture originates at the edge of the lithostatic compartment and extends into the low-pressure compartment.

of impermeable seals within the fault zone confines fluids at superhydrostatic to lithostatic pressures in compartments of various sizes and shapes. The size of these compartments is poorly constrained, although the vertical extent is limited to a few hundred meters [*Fournier*, 1991] and the horizontal extent is comparable [*Johnston*, 1994]. Observations of trapped fluid with high apparent pore pressure in exhumed faults provide some indication of compartment size. *Kerrich et al.* [1977] observed compartment sizes of up to 1 km. For currently active compartments, size may be inferred indirectly through near-surface strainmeter data. Strainmeters in 200-m-deep boreholes near the San Andreas fault in California operate at sensitivities of about 10^{-9}. Since strain changes above this measurement limit are not readily apparent in these data before large earthquakes [*Johnston et al.*, 1987], compartments at seismogenic depth could be as large as several hundred meters if rapid pressure changes occur at the kilobar level. For these reasons, we initially assume that compartments extend less than 1 km.

Equally important to this model is the pore pressure distribution in the fault zone. We may infer a probable pore pressure system from the heat flow measurements along the San Andreas fault. *Byerlee* [1992] provides an expression which relates the apparent coefficient of friction with the ratio of the pore pressure in the fault zone to the magnitude of the vertical stress. For a coefficient of friction, $\mu < 0.1$, implied by the absence of a heat flow anomaly over the fault, the average pore pressure in the fault zone must be 85% of lithostatic. If the fault zone consists exclusively of lithostatic and hydrostatic pore pressure compartments, 75% of the fault zone volume must be lithostatic pore pressure compartments. In other words, lithostatic compartments must contain 3 times the volume of hydrostatic compartments.

During differential plate motion, shear stress builds in the weak, fluid-filled fault zone until strong impermeable seals between high-pressure and low-pressure compartments rupture. Rupture of seals in response to tectonic loading would initiate shear fractures that propagate into the low-pressure compartment, enabling the rapid movement of fluid from the high-pressure compartment. Figure 1 illustrates the geometry of this process.

For this model we consider a relatively thin shear fracture in which fluid is constrained to flow primarily along fault strike in the direction of fracture propagation. The expression for one-dimensional transient flow of a compressible fluid through a porous medium is [*Brace et al.*, 1968]

$$\frac{\partial^2 P}{\partial x^2} = \frac{\eta\beta}{k}\left[\frac{\beta_{\text{eff}} - \beta_s}{\beta} + \varphi\left(1 - \frac{\beta_s}{\beta}\right)\right]\frac{\partial P}{\partial t} \tag{1}$$

where P is pressure in the fracture, η is dynamic viscosity, k is fracture permeability, φ is porosity, β is fluid compressibility, β_s is compressibility of the solid matrix, and β_{eff} is effective compressibility of the rock (as measured in a jacketed sample). For most rocks, β is much larger than either β_s or β_{eff} [*Brace et al.*, 1968]. Therefore the flow expression is

$$\frac{\partial^2 P}{\partial x^2} = \frac{\eta\beta\varphi}{k}\frac{\partial P}{\partial t}. \tag{2}$$

The shear fracture propagates into the low-pressure compartment. At any time in its evolution the fracture tip is dilatant. Analysis of exhumed faults shows dilatant behavior [*Sibson et al.*, 1988; *Chester et al.*, 1993] that may support this argument even though this is interpreted to result from fault irregularity. Thus the initial condition of the system $P(x, 0)$ is small since only the fracture tip is present at the time of fracture initiation.

In the *Byerlee* [1993] model the compartments are assumed to include the central fault gouge and the surrounding breccia zones. This region of a fault zone may be a kilometer thick and could contain substantial fluid volumes [*Cox et al.*, 1991]. By contrast, the shear fracture is only a few centimeters thick. Since the volume of the shear fracture is negligible compared to the volume of the high-pressure compartment, the pore pressure at the compartment boundary (where rupture first occurs) remains at the high-pressure levels for the duration of the process. In our extension of the Byerlee model we assume that the high-pressure compartment has lithostatic pore pressure levels. To simplify our mathematical analysis, we use the method of images, which essentially doubles the width of the low-pressure compartment, with a high-pressure compartment on either side. This is equivalent to reflection about the y axis in Figure 1. Thus the boundary condition is $P(\pm l, t) = P_L$.

Here we assume the pressure P approaches zero as the distance from the high-pressure compartment becomes rel-

atively large. This provides an approximation of the real behavior of the system. Applying Laplace transforms yields a pore pressure distribution in the shear fracture of

$$P(x, t) = P_L - P_L \text{ erf } (x/2(Dt)^{1/2}) \quad (3)$$

where $D = k/\eta\beta\varphi$. The pore pressure distribution is illustrated in Figure 2. In a more realistic description of the shear fracture evolution, $P \rightarrow 0$ as $x \rightarrow l$, and the average pore pressure in the fracture is hydrostatic. Because of the differences in formulation, equation (3) is only an approximation of the more realistic description.

This pore pressure distribution constantly evolves as the fracture propagates farther into the low-pressure compartment. The abrupt pore pressure change at the fracture tip causes a phase change, resulting in the rapid deposition of silica. In addition, the variation in pressure across the fracture, from near lithostatic at the rupture boundary to near-zero at the fracture tip, sharply reduces the silica solubility [*Fournier*, 1985; *Herrington and Wilkinson*, 1993; *Fournier and Potter*, 1982]. At a depth of 17 km the silica solubility across the fracture drops from 1 wt % near the lithostatic high-pressure compartment to less than 0.5 wt % at the fracture tip (see Figure 3). Consequently, silica deposition near the fracture tip may decrease permeability, reducing and perhaps stopping further fluid flow and fracture propagation. Should this happen, pressure builds in the fracture until rupture of the temporary seal occurs and the shear fracture propagation continues. This stop-and-start fracture propagation continues until the shear fracture is stopped or it reaches another high-pressure compartment. In the latter case, fluid will rush in from the newly breached high-pressure compartment and the pore pressure distribution in the fracture becomes quite complex. The shear fracture may continue to propagate along the fault through the high-pressure compartment, producing seismic radiation and moving at Rayleigh wave velocity [*Andrews*, 1976]. Should this fracture reach another impermeable seal between a high-pressure and low-pressure compartment, the seal ruptures and the entire process begins anew. Each time a seal ruptures or a shear fracture stops and starts, fluid motion occurs, possibly generating observable magnetic and electric field changes.

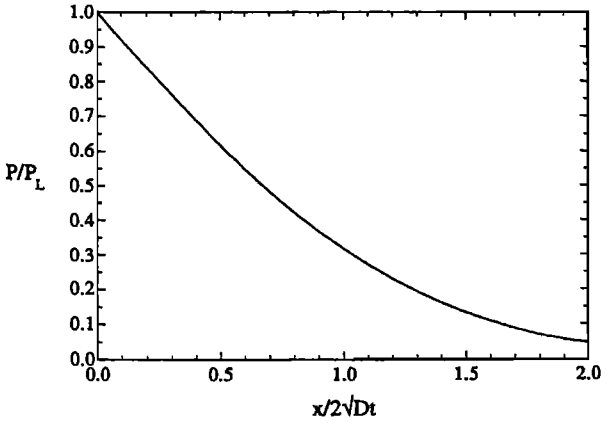

Figure 2. Normalized pore pressure distribution in the shear fracture as a function of distance and time. 95% of the total distribution occurs in the region $0 < x/2(Dt)^{1/2} < 1.36$.

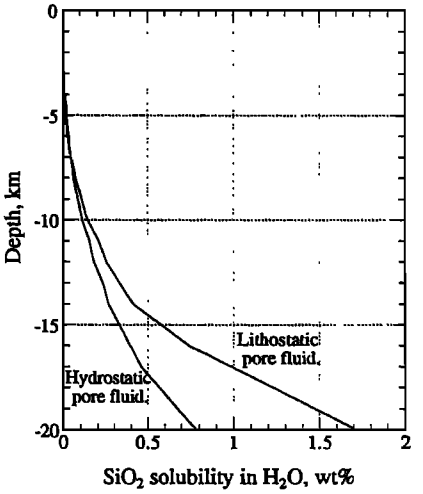

Figure 3. Solubility of silica in water by weight percentage versus depth on the San Andreas fault for hydrostatic and lithostatic pore pressure gradients (derived from *Fournier* [1985]).

Possible Mechanisms for ULF Emissions

There are three significant mechanisms for generation of ULF emissions that could result from the rupturing of an impermeable seal between high- and low-pressure compartments: magnetohydrodynamic (MHD), piezomagnetic, and electrokinetic effects. Both MHD and electrokinetic effects result from the fluid flow associated with the seal rupture. Piezomagnetism results from changes in magnetism produced by high pressures in the shear fracture.

In the case of magnetohydrodynamics the motion of an electrically conducting fluid in the presence of a magnetic field perturbs that field. The applied field here is simply Earth's magnetic field, and the other characteristics are defined by the fluid action in the fault zone. The magnetic Reynolds number Re_m provides an approximation of the perturbation of the magnetic field at the source. For our shear fracture model the MHD effect is negligible at the surface [*Fenoglio et al.*, 1994].

This result differs from that obtained by *Draganov et al.* [1991], who proposed an MHD model for the region surrounding the Loma Prieta earthquake in which a conductive sheet of water at 4 km depth moves with a fluid velocity of 40 mm/s. With this model he calculated a surface magnetic field of approximately 0.1 nT. The difficulties with this model concern the permeability of 10^{-10} m^2 proposed for this layer (i.e., equivalent of sand); the pressure gradient required to drive fluids at this velocity; the nonrealistic nature of sheet fluid flow with its implications for strain, seismicity, and surface hydrology; and the need to make this flow oscillatory with a wave number, k_x, of 10^{-4}, if this model is to approximate the electromagnetic signals observed by *Fraser-Smith et al.* [1990] for this earthquake. Even supposing a fracture system exists in this region, the permeability is unlikely to exceed 10^{-11} m^2 [*Brace*, 1980] under the most favorable of circumstances. With this permeability, the pressure gradient needed is 4×10^6 Pa/m. For this case, then, the pore pressure would be 4×10^{10} Pa. Thus the Draganov model requires a pore pressure well above lithostatic (about 10^8 Pa at 4 km depth), which is extremely

unlikely. We therefore conclude that magnetohydrodynamic effects at depth do not appear to contribute to anomalous surface magnetic fields.

The piezomagnetic effect results from a change in magnetization of ferromagnetic-bearing rock in response to applied stress. In our model, as the shear fracture propagates into the low-pressure compartment, the high pore pressures that act along the walls of the shear fracture produce piezomagnetic effects in the surrounding rock. We model this effect by treating the fracture as a dyke subject to stress equal to the pore pressure of the high-pressure compartment. Using numerical integration techniques, we can determine the magnetic field at the surface caused by the piezomagnetic effect [*Sasai*, 1991]. The result is a magnetic field that is everywhere less than 10^{-2} nT and is strongest directly over the source [*Fenoglio et al.*, 1994]. This contribution is additive to any magnetic field anomaly caused by electrokinetic effects.

The inadequacy of MHD and piezomagnetic effects to cause sizable (>1 nT) magnetic field anomalies at the surface for the shear fracture model leaves only electrokinetic effects as a possible mechanism for the generating large magnetic field anomalies. The following section describes the electrokinetic effect resulting from rapid fluid flow into a shear fracture created by a rupture between high- and low-pressure compartments.

Electrokinetic Effects

Electrokinetic effects are the electrical currents (and magnetic fields) generated by fluid flow through the crust in the presence of an electrified interface at the solid-liquid boundaries. This electrified interface consists of ions anchored to the solid phase, with an equivalent amount of ionic charge of opposite sign distributed in the liquid phase near the boundary. For a shear fracture into which fluid flows, this electrified interface exists at the fracture wall [*Overbeek*, 1953].

When the fluid in such a system moves, the charges in the fluid are transported along the fracture wall in the direction of fluid motion; that is, electric current exists. The current density and fluid flow are coupled processes described by the following equations [*Nourbehecht*, 1963; *Fitterman*, 1979]

$$\mathbf{j} = -\sigma \nabla E - \frac{\varepsilon \zeta}{\eta} \nabla P \tag{4}$$

and

$$\mathbf{v} = -\frac{\varepsilon \zeta}{\eta} \nabla E - \frac{k}{\eta} \nabla P \tag{5}$$

where $\mathbf{j}$ is current density, $\mathbf{v}$ is fluid velocity, E is streaming potential, ε is dielectric constant, ζ is zeta potential, and σ is fluid conductivity. The zeta potential is the measure of the initial potential (which exists because of a nonuniform distribution of the ions in the fluid phase) in the electrified interface.

The current density expressed in (4) has two components. The second term represents electric current resulting from mechanical energy being applied to the system and is sometimes called the "impressed" current. In our model this term describes current generated by fluid flow in the shear fracture. The electric field that develops as a passive response to this fluid flow sets up counter or "back" currents in the fluid and the surrounding fault zone depending on the distribution of electrical conductivity. The first term of (4) represents these back currents. The distribution of electrical conductivity determines what net magnetic fields result from these effects. At one extreme, as in the case of streaming potential (SP) measurements in the laboratory [*Ahmad*, 1964], insulated reservoirs of conducting fluid at different pressures are connected by an insulated pipe. Here the back currents are confined to the conducting fluid where they oppose the electric currents generated by fluid flow. This results in no net magnetic field.

The situation in our extension of the Byerlee fault model is very different. The conductivity and geometry of our model can be described in terms of an insulated reservoir of conducting fluid embedded in a less conducting fault zone of several kilometers thickness. Rupture of the reservoir allows fluid to flow in a stop-and-start fashion along shear cracks in the fault zone. The conductivity of the fluid (brine) is about 1 S/m, whereas the conductivity of the fault zone and its surroundings ranges from 0.3 to 0.001 S/m [*Eberhart-Phillips et al.*, 1990].

For this situation, the components of (4) can be viewed as two separate contributions to the overall electric current, given by

$$\mathbf{j} = \mathbf{j}_i + \mathbf{j}_b. \tag{6}$$

where $\mathbf{j}$ is the net electric current, $\mathbf{j}_i$ is the impressed current, and $\mathbf{j}_b$ is the back current. Within the high-pressure compartment, significant fluid flow occurs only near the rupture point. The impressed currents are small and are effectively cancelled by secondary back currents. While some current flow may result as a consequence of different ion mobilities, no significant magnetic field is generated.

Outside the compartment, fluid flows in the propagating shear fracture along the fault zone, which is neither hydrologically nor electrically isolated from the country rock. While the primary impressed currents resulting from this fluid flow are confined to a narrow shear fracture, back currents develop in the shear fracture and may also flow in the electrically conducting near-fault materials (volume currents).

The relative importance of the contributions of the net magnetic field from each of these two current systems is an important issue. To address the contribution from volume currents, we consider the special case where the material outside the fault is uniformly conducting with $\mathbf{j}$ vanishing at infinity. For this case, the field at r from the Biot-Savart law may be written [*Williamson and Kaufman*, 1981] as

$$\mathbf{B} = \frac{\mu_0}{4\pi} \int_v \frac{\nabla' \times \mathbf{j}(r')}{|r - r'|} \, dV. \tag{7}$$

where $\mathbf{B}$ is the magnetic field and μ_0 is the permeability of free space. This shows that the field is due to the geometrical aspect of the current system with a finite curl. Furthermore, since for uniform conductivity the volume current $\mathbf{j}_b$ is proportional everywhere to the gradient of the electric potential and since the curl of a gradient is zero, only the currents within the shear fracture give rise to a magnetic field. In our case, while the fault zone and near-fault conductivity structure is not uniform, it is reasonably so at the

depth at which the Loma Prieta earthquake occurred [*Eberhart-Phillips et al.*, 1990]. Thus we would expect the primary contribution to the magnetic field to be due to impressed currents in the fracture reduced by direct back current flow also within the fracture. The majority of the impressed current is cancelled by the the direct back current, but some current also flows in the surrounding conductive medium. Laboratory experiments involving flow of blood through conducting tissue indicate that measurable magnetic fields are generated by volume currents [*Williamson and Kaufman*, 1981]. These results are intriguing, although their applicability to earth materials is uncertain. Laboratory experiments of magnetic fields generated by flow of conducting fluids through fractured crustal rocks at seismogenic pressures and temperatures are clearly needed to determine the net current flow and relative importance of back current within a fracture. An exact solution will require a detailed knowledge of the conductivity of the material within and outside the fault zone, but presently, these data are not available. *Dobrovolsky et al.* [1989], *Mizutani et al.* [1976] and others have suggested that back currents may be ignored. We initially assume this to be the case to calculate an upper estimate of the magnetic fields generated for our model.

This simplifies our electrokinetic construct. We simply say the fluid within the fracture flows at approximately the same rate as the fracture propagates. Thus, when the fracture ceases propagation (and the fracture is entirely fluid filled; that is, soon after another high-pressure compartment is reached), the fluid flow will quickly cease and the electrokinetic effects end. Equilibrium is reestablished. Proceeding from these arguments, our current density is

$$\mathbf{j} = \hat{a}_x \frac{P_L \varepsilon \zeta}{\eta (Dt)^{1/2}} e^{-x^2/4Dt}. \tag{8}$$

This current density in the shear fracture generates a magnetic field at the surface. We apply the Biot-Savart law to determine the magnetic field.

$$\mathbf{B} = \frac{\mu_0}{4\pi}\int_A \frac{\mathbf{j} \times \mathbf{r}}{r^2}\, dA$$

$$= \frac{\mu_0 j_0}{4\pi (t)^{1/2}} \int_0^l \int_d^{d+h} \left(-\frac{z - z'}{r^3}\, \hat{\mathbf{a}}_y + \frac{y}{r^3}\, \hat{\mathbf{a}}_z \right)$$

$$\cdot \exp\left[\frac{-(x - x')^2}{4Dt}\right] dz'\, dx' \tag{9}$$

Table 1. Constants Important for Electrokinetic Effects

Variable	Value
ε, dielectric constant	7.07×10^{-10} F/m
ζ, zeta potential	0.1 V
β, fluid compressibility	3×10^{-10} Pa^{-1}
φ, porosity	0.5
η, dynamic viscosity	10^{-4} Pa s
μ_0, magnetic permeability of free space	$4\pi \times 10^{-7}$ H/m
k, fracture permeability	10^{-12} m^2
ρ, density of rock	2500 kg/m^3
l, fracture length	200 m
d, depth to the top of the fracture	17 km
h, height of fracture	1000 m

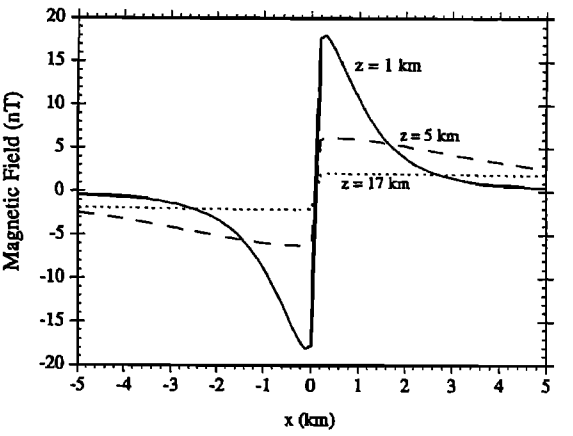

Figure 4. Comparison of the horizontal magnetic field along fault strike generated by fluid flow in a shear fracture 200 m long and 1000 m high buried at 1 km, 5 km, and 17 km (at time t = 1 s).

where $r = [(x - x')^2 + y^2 + (z - z')^2]^{1/2}$, $j_0 = P_L \varepsilon \zeta / \eta (D)^{1/2}$, and μ_0 is the magnetic permeability of free space. The magnetic field cannot be determined analytically from this integral expression. We can integrate with respect to the vertical variable z' to reduce the problem to a single integral. Using integration by parts allows numerical integration that reveals the horizontal magnetic field B_y to be several orders of magnitude larger than the vertical magnetic field B_z. Therefore we will limit our analysis to the horizontal magnetic field at the surface.

For a current sheet 200 m in length and 1000 m in height, the surface magnetic field can be calculated for different depths and times using the physical constants summarized in Table 1. Figures 4 and 5 show the magnetic field profiles along fault strike for varying depths and times, respectively. As the depth of the source increases, the peak magnetic value decreases and the signal becomes more and more spatially distributed. As time increases, the magnetic field decreases rather uniformly along fault strike. The curve labeled t = 1 s in Figure 5 corresponds to the curve labeled z = 17 km in Figure 4.

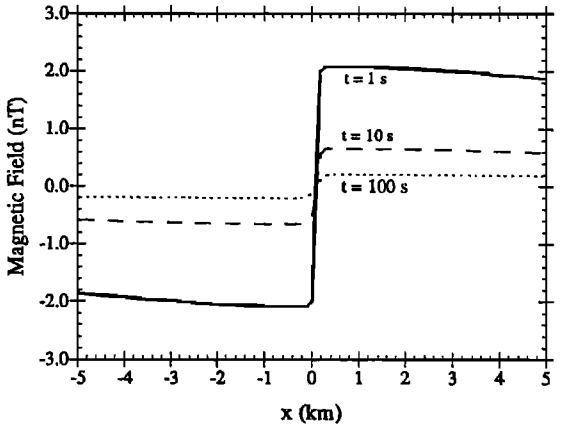

Figure 5. Horizontal magnetic field evolution along fault strike generated by fluid flow in a shear fracture 200 m long and 1000 m high buried at 17 km. The evolution is shown at times t = 1, 10, and 100 s.

For the modestly sized source considered, the magnetic field at the surface may be as high as ±2 nT even for a source buried at 17 km. Clearly, electrokinetic effects resulting from rupture of impermeable layers between fault compartments of differing pore pressure may be quite large.

Discussion of the Loma Prieta Earthquake ULF Observations

Of the mechanisms considered, electrokinetic effects generate the strongest magnetic field at the surface associated with a shear fracture driven by high pore pressures in response to failure of an impermeable layer between fault zone compartments. The October 17, 1989, Loma Prieta M_L 7.1 earthquake offers a unique opportunity to test the validity of the fracture propagation model. Before and after this earthquake an ultralow frequency (ULF) magnetometer operated in Corralitos, California, only 7 km from the epicenter of the mainshock. This instrument indicated a number of ULF magnetic field fluctuations recorded as spectral peaks throughout its 0.01- to 10.0-Hz bandwidth [*Fraser-Smith et al.*, 1990]. Within the ULF range, the 0.01- to 0.02-Hz frequency window showed the most remarkable signals, with barely perceptible changes in the 5.0- to 10.0-Hz bandwidth.

The primary focus of this paper is to determine whether the evolution of the compartment model proposed by *Byerlee* [1993] can generate magnetic signals large enough to account for the observations of *Fraser-Smith et al.* [1990]. Specifically, we wish to examine two major increases in the magnetic field of October 1989, one on October 5, 1989, and the other just 3 hours prior to the mainshock. In the 0.01- to 0.02-Hz bandwidth, the magnitudes were 2.0 nT for the first and 6.7 nT for the second.

The static considerations of the previous sections illustrate that electrokinetic effects generate signals comparable with the largest changes in the Fraser-Smith et al. data. The question becomes how to explain the oscillatory nature of the signals. For the geometry of the fault zone described by *Byerlee* [1993], these oscillations can occur in two significant ways, as mentioned in the fault model section. The first is a stop-and-start propagation of the fracture within the low-pressure compartment. This mechanism is triggered because of the tremendous decrease in pore pressure from the rupture in the impermeable boundary between compartments to the fracture tip. This pressure decrease results in reduced solubility and deposition of silica in the fracture. With enough deposition the fracture may be sealed and propagation ceases. With the end of fluid motion the electrokinetic effects also cease. The pressure in the newly sealed fracture rapidly rises to lithostatic levels, the new seal ruptures, and the process repeats. This process continues to repeat until the next lithostatic compartment is reached. Upon reaching the next lithostatic compartment the deformation propagates at shear wave velocity to the next impermeable seal between high- and low-pressure compartments. The full process repeats itself again.

The length of the fracture determines the time it takes for the fracture to propagate that distance. If we assume that the fluid pressure rises virtually instantaneously to lithostatic levels once the fracture seals or is partially blocked by silica deposition, then the fracture propagation time is equal to the period of oscillation for this intermediate stage. We can derive a relation between propagation time and fracture distance using the pore pressure distribution in the shear fracture (see Figure 2). The pore pressure expression (3) is a complimentary error function which asymptotically approaches zero as the horizontal variable approaches infinity. The region which covers 95% of the pore pressure distribution is $0 < x/2(Dt)^{1/2} < 1.36$ (see Figure 2). This area represents an approximation of the finite length fracture. Under this assumption, if we consider that silica deposition and initiation of the stop and start mechanism occur at the rightmost point of the 95% distribution, we can find an expression which relates fracture length l and propagation time T:

$$l/2(DT)^{1/2} = 1.36 \tag{10a}$$

or

$$T = l^2/7.4D. \tag{10b}$$

Since T is also the period of oscillation, the frequency window corresponding to a particular fracture length is simply $1/T$.

Table 2. Relationship of Frequency Window and Fracture Length

Frequency, Hz	Period, s	Fracture Length, m
0.01–0.02	50–100	157–222
0.02–0.05	20–50	99–157
0.05–0.10	10–20	70–99
0.1–0.2	5–10	50–70
0.2–0.5	2–5	31–43
0.5–1.0	1–2	22–31
1.0–2.0	0.5–1	16–22
2.0–5.0	0.2–0.5	9.9–16
5.0–10.0	0.1–0.2	7.0–9.9

The strain data and exhumed fault observations, along with determinations of average pore pressure in the fault zone, limit the compartment size and geometry. For equal width and height of the lithostatic and hydrostatic compartments, the hydrostatic compartments must be one-third the length of lithostatic compartments. Since the electrokinetic effects occur only in the low-pressure compartments, the maximum fracture length would be about 300 m. For this case, we ignore stop-and-start fracture propagation in the low-pressure compartment and consider only the repetition as the fracture propagates along the fault. The period of oscillation is about 180 s, which corresponds to a frequency of 0.006 Hz. This frequency is between the ULF range (0.01–10.0 Hz) and the sampling frequency (0.0016 Hz) of strainmeters. Consequently, accepting the veracity of the Fraser-Smith et al. data places an additional constraint on the compartment size vis-a-vis the fracture propagation rates.

Table 2 shows the fracture lengths which correspond to each frequency band in the ULF range. Consider the 0.5- to 1.0-Hz bandwidth, with associated fractures of about 20–30 m in length. In the magnetic data recorded at Corralitos, the last obvious disturbances occur in this frequency window. Suppose that a 25-m fracture repeatedly forms within the low-pressure compartment until reaching the next high-pressure compartment. For a 200-m-long low-pressure compartment, eight such fractures will form, generating a repeat-

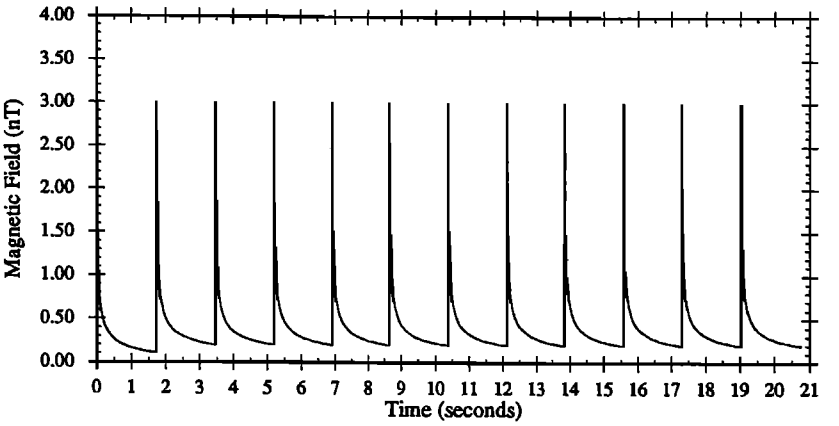

Figure 6. Horizontal magnetic field for 25-m fractures as seen by a surface observer 17 km above the initial rupture. This magnetic field arises from the current associated with fluid flow into a 200 m by 1000 m shear fracture.

ing magnetic signature., Figure 6 shows the magnetic field time series for an observer standing 17 km directly above the rupture between the high- and low-pressure compartments. Figure 7 shows the power spectrum which results from this repeated signal. The most obvious and important feature of the power spectrum is the increasing strength of the signal as frequency decreases. This matches the general character of the magnetic data recorded by *Fraser-Smith et al.* [1990].

Conclusions

This investigation of magnetic effects associated with the evolution of the compartment fault model proposed by *Byerlee* [1993] yields several interesting results. Most importantly, the rupture of brittle impermeable layers between compartments of different pore pressure regimes in response to tectonic loading leads to shear fracture formation in the low-pressure compartment. Extremely turbulent fluid flow into the shear fracture generates magnetic signals measurable at the surface as a result of electrokinetic effects. Other mechanisms, such as piezomagnetism and magnetohydrodynamics, contribute negligibly to the overall magnetic field.

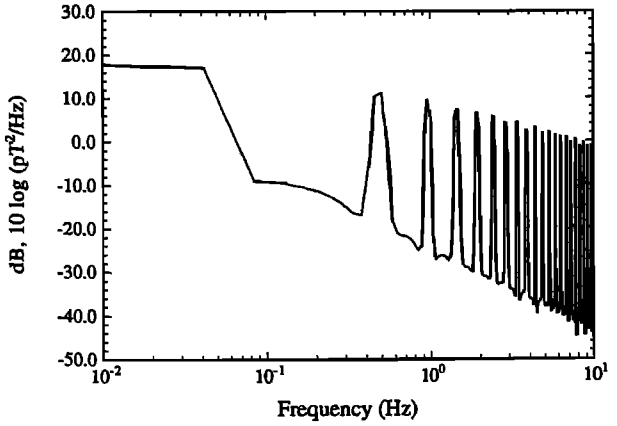

Figure 7. Power spectrum for the time series in Figure 6. The general characteristics of this plot are similar to the energy distribution in the magnetic data recorded by *Fraser-Smith et al.* [1990].

Stop-and-start fracture propagation, a consequence of the spatial distribution of the pore pressure within the shear fracture, may explain the short-period ULF signals recorded prior to the Loma Prieta earthquake. If this mechanism generated these measured signals, segments of the fault of perhaps several kilometers in extent were failing largely aseismically during this time. The cumulative effects of such large-scale aseismic failure could have been detected on a strain array over the area had one existed at the time. Further, some increase in microseismicity should also have occurred, though none was apparent during the period prior to the Loma Prieta earthquake [*White*, 1993].

The aftershock record of the Loma Prieta earthquake shows no strong correlation between seismic events and magnetic field fluctuations [*Fenoglio et al.*, 1993]. However, the highest correlation levels in the comparison occurred for coincident aftershocks and magnetic signals. Given that the compartment failure mechanism can trigger earthquakes, it is not unexpected that the aftershocks, occurring in an already weakened and deformed region, are coincident with magnetic field changes that might result from further fluid flow in response to continuing failure of the brittle impermeable layers between compartments.

Strain constraints [*Johnston et al.*, 1990] and exhumed fault observations limit the size of the high-pressure compartments to less than 1 km in extent. By inference from the average pore pressure within the fault zone, the low-pressure compartments are only one-third the extent of the high-pressure compartments. Even for low-pressure compartments only 200 m across, the electrokinetic effects at the surface are similar in magnitude to the recorded magnetic field data. This being the case, the compartment fault model appears capable of satisfying the ULF observations associated with the Loma Prieta earthquake.

Acknowledgments. We thank Dave Fitterman and Bill Stuart for reviews of an earlier version of the paper. We also thank the reviewers Steve Park and Ted Madden and the Associate Editor Rick Sibson for helpful comments regarding the fault zone dynamics and the electric current system.

References

Ahmad, M., A laboratory study of streaming potentials, *Geophys. Prospect.*, *12*, 49–64, 1964.

Andrews, D. J., Rupture velocity of plane strain shear cracks, *J. Geophys. Res.*, *81*, 5679–5687, 1976.

Brace, W. F., Permeability of crystalline and argillaceous rocks, *Int. J. Rock Mech.*, *17*, 876–893, 1980.

Brace, W. F., J. B. Walsh, and W. T. Frangos, Permeability of granite under high pressure, *J. Geophys. Res.*, *73*, 2225–2236, 1968.

Byerlee, J., Friction, overpressure and fault normal compression, *Geophys. Res. Lett.*, *17*, 2109–2112, 1990.

Byerlee, J., The change in orientation of subsidiary shears near faults containing high pore fluid pressure, *Tectonophysics*, *211*, 295–303, 1992.

Byerlee, J., Model for episodic flow of high pressure water in fault zones before earthquakes, *Geology*, *21*, 303–306, 1993.

Chester, F. M., J. P. Evans, and R. L. Biegel, Internal structure and weakening mechanisms of the San Andreas fault, *J. Geophys. Res.*, *98*, 771–786, 1993.

Cox, S. F., V. J. Wall, M. A. Etheridge, and T. F. Potter, Deformational and metamorphic processes in the formation of mesothermal vein-hosted gold deposits—Examples from the Lachlan Fold Belt in central Victoria, Australia, *Ore Geol. Rev.*, *6*, 391–423, 1991.

Dobrovolsky, I. P., N. I. Gershenzon, and M. B. Gokhberg, Theory of electrokinetic effects occurring at the final stage in the preparation of a tectonic earthquake, *Phys. Earth Planet. Inter.*, *57*, 144–156, 1989.

Draganov, A. B., U. S. Inan, and Y. N. Taranenko, ULF magnetic signatures at the Earth due to groundwater flow: A possible precursor to earthquakes, *Geophys. Res. Lett.*, *18*, 1127–1130, 1991.

Eberhart-Phillips, D., V. F. Labson, W. D. Stanley, A. J. Michael, and B. D. Rodriguez, Preliminary velocity and resistivity models of the Loma Prieta earthquake region, *Geophys. Res. Lett.*, *17*, 1235–1238, 1990.

Fenoglio, M. A., A. C. Fraser-Smith, G. C. Beroza, and M. J. S. Johnston, Comparison of ultra-low frequency electromagnetic signals with aftershock activity during the 1989 Loma Prieta earthquake sequence, *Bull. Seismol. Soc. Am.*, *83*, 347–357, 1993.

Fenoglio, M. A., M. J. S. Johnston, and J. Byerlee, Magnetic and electric fields associated with changes in high pore pressure in fault zones—Application to the Loma Prieta ULF emissions, *U.S. Geol. Surv. Open File Rep.*, *94-228*, 262–278, 1994.

Fitterman, D. V., Electrokinetic and magnetic anomalies associated with dilatant regions in a layered Earth, *J. Geophys. Res.*, *83*, 5923–5928, 1978.

Fitterman, D. V., Theory of electrokinetic-magnetic anomalies in a faulted half-space, *J. Geophys. Res.*, *84*, 6031–6040, 1979.

Fitterman, D. V., and T. R. Madden, Resistivity observations during creep events at Melendy Ranch, California, *J. Geophys. Res.*, *82*, 5401–5408, 1977.

Fournier, R. O., Continental scientific drilling to investigate brine evolution and fluid circulation in active hydrothermal systems, in *Observation of the Continental Crust Through Drilling I*, edited by C. B. Raleigh, pp. 98–122, 1985.

Fournier, R. O., The transition from hydrostatic to greater than hydrostatic fluid pressures in presently active continental hydrothermal systems in crystalline rock, *Geophys. Res. Lett.*, *18*, 955–958, 1991.

Fournier, R. O., and R. W. Potter II, An equation correlating the solubility of quartz in water from 25° to 900°C at pressures up to 10,000 bars, *Geochem. Cosmochem. Acta*, *46*, 1969–1973, 1982.

Fraser-Smith, A. C., A. Bernardi, P. R. McGill, M. E. Ladd, R. A. Helliwell, and O. G. Villard Jr., Low-frequency magnetic field measurements near the epicenter of the M_s 7.1 Loma Prieta earthquake, *Geophys. Res. Lett.*, *17*, 1465–1468, 1990.

Herrington, R. J., and J. J. Wilkinson, Colloidal gold and silica in mesothermal vein systems, *Geology*, *21*, 539–542, 1993.

Ishido, T., and H. Mizutani, Experimental and theoretical basis of electrokinetic phenomena in rock-water systems and its application to geophysics, *J. Geophys. Res.*, *86*, 1763–1775, 1981.

Johnston, M. J. S., Review of magnetic and electric field effects near active faults and volcanoes in the U.S.A., *Phys. Earth Planet. Inter.*, *57*, 47–63, 1989.

Johnston, M. J. S., Nucleation size of moderate earthquakes and kinematics of the San Andreas Fault in California from submicro Hz to 30 Hz strain measurements, paper presented at IASPEI 27th General Assembly Meeting, Int. Assoc. of Seismol. and Phys. of the Earth's Inter., Wellington, New Zealand, 1994.

Johnston, M. J. S., A. T. Linde, M. T. Gladwin, and R. D. Borcherdt, Fault failure with moderate earthquakes, *Tectonophysics*, *144*, 189–206, 1987.

Johnston, M. J. S., A. T. Linde, and M. T. Gladwin, Near-field high resolution strain measurements prior to the October 18, 1989, Loma Prieta M_s 7.1 earthquake, *Geophys. Res. Lett.*, *17*, 1777–1780, 1990.

Kerrich, R., W. S. Fyfe, and I. Allison, Iron reduction around gold-quartz veins, Yellowknife District, Northwest Territories, Canada, *Econ. Geol.*, *72*, 657–663, 1977.

Madden, T. R., Electrical measurements as stress-strain monitors, *U.S. Geol. Surv. Open File Rep.*, *79-0370*, 301–347, 1979.

Mazella, A., and H. F. Morrison, Electrical resistivity variations associated with earthquakes on the San Andreas fault, *Science*, *185*, 855–857, 1974.

Miyakoshi, J., Anomalous time variation of the self-potential in the fractured zone of an active fault preceding the earthquake occurrence, *J. Geomagn. Geoelectr.*, *38*, 1015–1030, 1986.

Mizutani, H., T. Ishido, T. Yokokura, and S. Ohnishi, Electrokinetic phenomena associated with earthquakes, *Geophys. Res. Lett.*, *13*, 365–368, 1976.

Morrison, H. F., R. Fernandez, and R. F. Corwin, Earth resistivity, self-potential variations, and earthquakes: A negative result for $M = 4.0$, *Geophys. Res. Lett.*, *6*, 139–142, 1979.

Nadeau, R., M. Antilok, P. Johnson, W. Foxall, and T. V. McEvilly, Seismological studies of Parkfield, III, Microearthquake clusters in the study of fault-zone dynamics, *Bull. Seismol. Soc. Am.*, *84*, 247–263, 1994.

Nourbehecht, B., Irreversible thermodynamic effects in inhomogeneous media and their applications in certain geoelectric problems, Ph.D. thesis, Mass. Inst. of Technol., Cambridge, 1963.

Overbeek, J. T., Thermodynamics of electrokinetic phenomena, *J. Colloid Sci.*, *8*, 420, 1953.

Park, S. K., and D. V. Fitterman, Sensitivity of the telluric monitoring array in Parkfield, California, to changes of resistivity, *J. Geophys. Res.*, *95*, 15,557–15,571, 1990.

Qian, F., Y. Zhao, M. Zu, Z. Wang, X. Liu, and S. Chang, Geoelectric resistivity anomalies before earthquakes, *Sci. Sin., Ser. B*, *26*, 326–336, 1983.

Rice, J. R., Fault Stress States, Pore pressure distributions, and the weakness of the San Andreas fault, in *Earthquake Mechanics and Transport Properties of Rocks*, edited by B. Evans and T.-F. Wong, pp. 475–503, Academic, San Diego, Calif., 1992.

Sasai, Y., Application of the elasticity theory of dislocation to tectonomagnetic modeling, *Bull. Earthquake Res. Inst. Univ. Tokyo*, *55*, 387–447, 1980.

Sasai, Y., Tectonomagnetic modeling on the basis of the linear piezomagnetic effect, *Bull. Earthquake Res. Inst. Univ. Tokyo*, *66*, 585–722, 1991.

Sheng, P., and Z. Chen, Local-field distribution in random dielectric media, *Phys. Rev. Lett.*, *60*, 2277, 1988.

Sibson, R. H., F. Robert, and K. H. Poulsen, High-angle reverse faults, fluid-induced pressure cycling, and mesothermal gold-quartz deposits, *Geology*, *16*, 551–555, 1988.

Stacey, F. D., The seismomagnetic effect, *Pure Appl. Geophys.*, *58*, 5–22, 1964.

Stacey, F. D., and M. J. S. Johnston, Theory of the piezomagnetic effect in titanomagnetic-bearing rocks, *Pure Appl. Geophys.*, *97*, 146–155, 1972.

White, R. A., The Loma Prieta, California earthquake of October 17, 1989—Preseismic observations, *U.S. Geol. Surv. Prof. Pap.*, *1550-C*, 1993.

Williamson, S. J., and L. Kaufman, Biomagnetism, *J. Magn. Magn. Mater.*, *22*, 129–201, 1981.

J. D. Byerlee and M. J. S. Johnston, U.S. Geological Survey, 345 Middlefield Road, MS 977, Menlo Park, CA 94025. (e-mail: mal@the beach.wr.usgs.gov)

M. A. Fenoglio, Geophysics Department, Stanford University, Stanford, CA 94305. (e-mail: markf@pangea.stanford.edu)

(Received February 23, 1994; revised January 9, 1995; accepted January 9, 1995.)